Depinning of three-dimensional drops from wettability defects

Ph. Beltrame[1(a)], P. Hänggi[1] and U. Thiele[2]

[1] *Institut für Physik, Universität Augsburg - D-86135 Augsburg, Germany*
[2] *Department of Mathematical Sciences, Loughborough University - Loughborough, Leicestershire, LE11 3TU, UK*

Introduction. – Drops sliding along a solid substrate under the influence of a lateral force are a very common physical phenomenon. The force might be gravity for drops on an inclined or vertical wall, centrifugal forces for drops on a rotating disk or external shear for drops in an ambient flow. Note that lateral gradients in wettability, temperature or electrical fields can as well drive sliding motion. For smooth homogeneous substrates, an arbitrarily small driving force results in drops that move with constant velocity and shape [1–3]. Larger driving forces may lead to shape instabilities, *e.g.*, trailing cusps may evolve that periodically emit small satellite drops [1,4].

Real substrates, however, are normally not smooth. They are rough or have local chemical or topographical defects. Even microscopic defects can have a strong influence on the drop dynamics. The heterogeneities may cause stick-slip motion [5,6] or roughening [7,8] of moving contact lines, and are thought to be responsible for contact angle hysteresis [9–12]. A local variation of the driving force (*e.g.*, electrostatic field or temperature gradient) may play the same role as a substrate defect.

The present paper focuses on the depinning of three-dimensional (3d) drops from hydrophobic and hydrophilic line defects that pin them at their front and back, respectively: A hydrophobic defect is less wettable for the drop that therefore has to be forced to pass over it. On the contrary, a hydrophilic defect is more wettable and the drop has to be forced to leave it as sketched in fig. 1. A recent theoretical study of the depinning dynamics of two-dimensional (2d) drops corresponding to 3d ridges with imposed transverse translational symmetry finds stick-slip motion beyond depinning [13,14].

The present work is based on a thin film evolution equation in long-wave approximation [15,16] that incorporates wettability in the form of a disjoining pressure [9]. It models the effective molecular interactions between the substrate and the free surface of the liquid, *e.g.*, long-range apolar van der Waals interactions and short-range polar electrostatic or entropic interactions [17]. With the proper choice of terms, such a disjoining pressure describes drops of partially wetting liquid with a small equilibrium contact angle that coexist with an ultra-thin precursor film. An advantage of such a model is the absence of a contact line singularity. Incorporating wettability in such a way allows one to study the influence of chemical substrate heterogeneities or defects by a spatial modulation of the involved material parameters. Note, however, that they have to vary on length scales much larger than the film thickness to be consistent with the long-wave approximation [18]. The presented analysis of the behaviour of 3d drops is based on a study of i) steady drops and their stability and ii) the stick-slip motion of droplets beyond depinning. Both are based on recently developed effective algorithms for the continuation of pinned steady drops described by a partial differential equation and the time simulation of the dynamics of sliding drops [19].

(a) E-mail: Philippe.Beltrame@physik.uni-augsburg.de

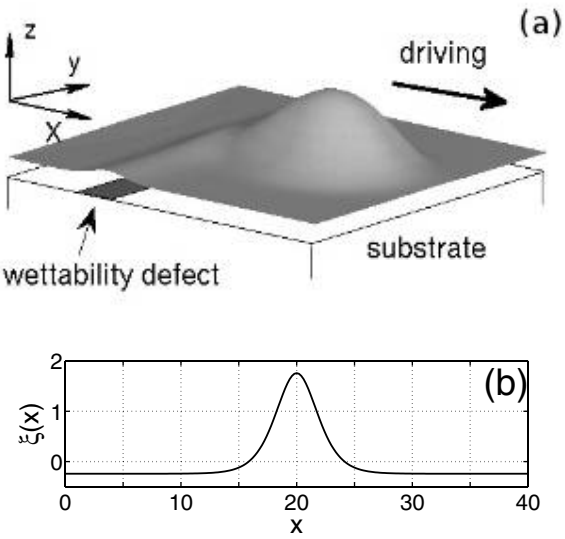

Fig. 1: Panel (a) gives a sketch of the considered three-dimensional geometry: a drop on a heterogeneous substrate and under a driving force μ along the x-direction. The wettability is assumed to depend on the x-direction only. (b) The employed heterogeneity profile $\xi(x)$ as defined by eq. (3) in terms of Jacobi elliptic functions is shown for $k = 1 - 10^{-6}$ and $L_x = 40$. It corresponds to a localised wettability defect.

Model and numerical method. – We consider a liquid layer or drop on an inhomogeneous two-dimensional solid substrate as sketched in fig. 1. The liquid partially wets the substrate (with a small equilibrium contact angle) and is subject to a small constant lateral force μ that acts in the x-direction. Employing long-wave approximation, the dimensionless evolution equation for the film thickness profile $h(x, y, t)$ is derived from the Navier-Stokes equations, continuity and boundary conditions (no-slip at substrate, force equilibria at free surface) [15,16]. It reads

$$\partial_t h = -\nabla \cdot \{m(h) \left[\nabla \left(\Delta h + \Pi(h, x)\right) + \mu \mathbf{e}_x\right]\}, \qquad (1)$$

where $\nabla = (\partial_x, \partial_y)$ and $\Delta = \partial_{xx} + \partial_{yy}$ are the planar gradient and Laplace operator, respectively. The mobility function $m(h) = h^3$ corresponds to Poiseuille flow and Δh represents the Laplace pressure (capillarity). Note that the ratio of the used length scales vertical and parallel to the substrates corresponds roughly to the small equilibrium contact angle. This implies that contact angles in the dimensionless models may be of order one. The disjoining pressure $\Pi(h, x)$ models the position-dependent wetting properties that in the case of transverse line defects only depend on the x-direction. The literature discusses many different functional forms for $\Pi(h)$ [9,20]. Most model the presence of an ultra-thin precursor film of about 1–10 nm thickness and thereby avoid a "true" film rupture. We employ long-range apolar van der Waals interactions combined with a short-range polar interaction [9,17,21]

$$\Pi(h, x) = \frac{b}{h^3} - [1 + \epsilon\xi(x)]\, e^{-h}, \qquad (2)$$

where ϵ and $\xi(x)$ are the amplitude and profile of the heterogeneity, respectively. To model a periodic array of localised defects, $\xi(x)$ is based on Jacobi elliptic functions. In particular, we employ

$$\xi(x) = \{2\,\mathrm{cn}[2K(k)x/L_x, k]\}^2, \qquad (3)$$

where $K(k)$ is the complete elliptic integral of the first kind. As $k \to 1$, eq. (3) describes localised defects. The period L_x is chosen sufficiently large to avoid interactions between subsequent drops/defects. Throughout the paper, k is fixed to $1 - 10^{-6}$ and $L_x = 40$. The employed profile $\xi(x)$ is given in fig. 1. The amplitude ϵ represents the wettability contrast. For $\epsilon < 0$ [$\epsilon > 0$], the defect is less [more] wettable than the surrounding substrate, *i.e.*, the defect is hydrophobic [hydrophilic]. The imposed spatial periodicity allows one to characterise stick-slip motion by its period in time.

Based on eq. (1) with (2) the depinning behaviour in the 3d case is analysed as follows: Steady-state solutions (pinned drops) and their stability are determined using continuation techniques and the stick-slip motion beyond the depinning threshold is analysed using time-stepping algorithms. Note that in the 2d case [13,14] an explicit scheme suffices for the latter and continuation can be performed using the package AUTO [22]. This is not possible in the 3d case where an effective and exact time simulation of eq. (1) is challenging and leads to a number of numerical problems [4,23,24]. Here, we employ an approach based on exponential propagation [25]. It allows for a very good estimate of the optimal timestep for the different regimes of the dynamics. This is of paramount importance as close to the depinning transition typical time scales vary over many orders of magnitude. The second advantage lies in the possibility to adapt the scheme in such a way that it can be used to continue branches of steady drop states and to determine their stability [19].

Results and discussion. – Without lateral force ($\mu = 0$) and for fixed volume, there exists a unique stable drop solution for each wettability contrast ϵ. The drop sits on top of a hydrophilic defect or between hydrophobic defects. Other normally unstable steady solutions may exist [26]. Increasing the lateral driving force μ from zero, the drop does not start to slide as for a homogeneous substrate [2], but remains pinned by the defect. A hydrophobic defect blocks the drop at the front, it becomes compressed and increases its height until it finally depins. In contrast, a hydrophilic defect holds a drop at its back. With increasing driving, it stretches and decreases its height until it depins. The mechanism of depinning was already studied in the case of a 2d drop (3d ridge) [13,14].

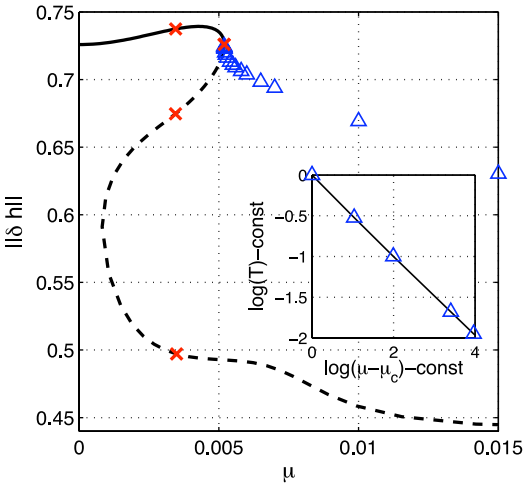

Fig. 2: (Colour on-line) Bifurcation diagram for 3d drops pinned by a hydrophilic line defect of strength $\epsilon = -0.3$. Shown is the (time-averaged) L^2 norm $\| \delta h \|$ of steady and time-periodic solutions as a function of the lateral driving force μ. Branches of stable pinned drops and unstable steady solutions correspond to solid and dashed lines, respectively. Triangles represent sliding drops performing a stick-slip motion beyond depinning. The domain size is 40×40 and the mean liquid height is $H = 1$. Crosses indicate profiles given in fig. 3. The inset gives for the stick-slip motion the dependence of the time-period on $\mu - \mu_c$. The straight line corresponds to a power law with exponent $-1/2$.

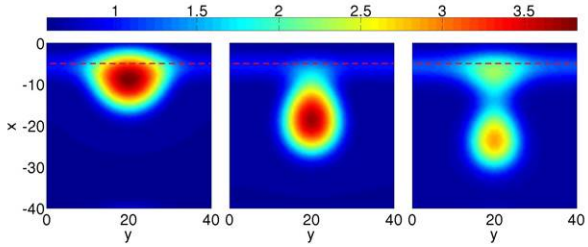

Fig. 3: (Colour on-line) Shown are contours of steady-drop solutions for a hydrophilic defect for $\mu = 3.5 \cdot 10^{-3}$. From left to right, profiles correspond to crosses in fig. 2 from large to small norm, *i.e.*, the left panel shows the stable pinned drop. The thin line marks the maximum of wettability.

A stable pinned ridge ceases to exist at a saddle-node bifurcation at μ_c. For larger μ, one finds a periodic stick-slip motion: the ridge stays close to one defect for a long time before it slides fast to the next one. A square root dependence of the inverse period on $\mu - \mu_c$ suggests that depinning occurs *via* a Saddle Node Infinite PERiod (SNIPER) bifurcation.

We now consider truly 3d drops as sketched in fig. 1, *i.e.*, we lift the restriction of the imposed translational invariance in y-direction used in the case of ridges (2d drops) [13]. Figure 2 shows the bifurcation diagram for a single drop pinned by a hydrophilic line defect with strength $\epsilon = -0.3$. Although at first glance the diagram looks similar to the 2d case (*e.g.*, fig. 20 of [13]), the results differ in important details due to the additional degrees of freedom. Without driving ($\mu = 0$), the drop sits symmetrically on the defect with an elliptic contour that has its long axis on the defect (not shown). When increasing μ, the drop shifts to the downstream side of the defect where it is retained by the high wettability patch below its tail. The drop stretches downstream but is compressed transversally. As a result the norm increases (contrary to the 2d case). The stable drop loses its stability *via* a saddle-node bifurcation at the critical driving $\mu_c = 5.193 \cdot 10^{-3}$. An unstable branch continues backwards towards smaller μ and turns again at a further saddle-node bifurcation. The resulting branch of lowest norm then continues towards large μ. Its properties strongly differ from the 2d case and will be discussed below. A selection of steady stable and unstable drop solutions (crosses in fig. 2) is presented in fig. 3. The left panel shows the stable pinned drop whereas the middle one represents an unstable drop that is connected to the hydrophilic patch only by an almost cusp-like thin bridge that seems to be at the point of breaking. Physically, it corresponds to a threshold solution: If the drop is moved a bit upstream [downstream], it retracts [slips to the next defect] and converges to the stable drop solution. The right panel, finally, gives the unstable solution of lowest norm. It resembles two drops joined by a thin thread with the smaller one sitting on the heterogeneity.

Beyond depinning ($\mu > \mu_c$), no stable steady drops exist and we expect a time-dependent behaviour. In the present spatially periodic setting drops depin from one defect and slide to the next one. There, however, they do not stop entirely but slow down as the defect tries to retain them. The time-averaged norm for several μ is given in fig. 2 and one can well appreciate that the corresponding solution branch emerges from the saddle-node bifurcation at μ_c. This together with the square root dependence of the inverse time-period (mean sliding speed) on $\mu - \mu_c$ shown in the inset of fig. 2 indicates that it is actually a Saddle Node Infinite PERiod (SNIPER) bifurcation [13]. A time series of snapshots for the stick-slip motion of a single drop is given in fig. 4. Note that the respective times are not equidistant. It takes the drop about 25000 time units to slowly stretch away from the defect (snapshots 1 and 2). Then within 500 units it depins and slides to the next defect (snapshots 2 to 5), where it needs another 25000 units to reach an identical state as in snapshot 1 (snapshots 5 and 6). Unlike the 2d case, the depinning itself resembles a pinch-off event at a water tap: the bridge between drop and a "reservoir" on the hydrophilic stripe becomes thinner until it snaps. Once the main drop slides, a small drop remains behind on the defect. The particular ratio of stick/stretch and slip phase is about 50 : 1. It diverges when approaching the bifurcation.

The bifurcation diagram for the case of a hydrophobic defect with $\epsilon = 0.3$ is given in fig. 5. A stable pinned drop is blocked at its front by the defect (solid line).

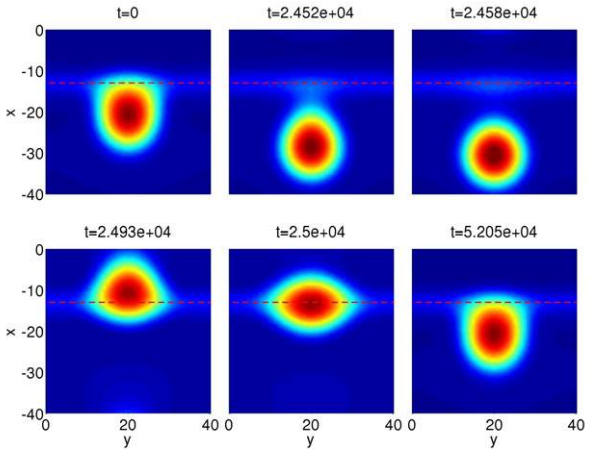

Fig. 4: (Colour on-line) Snapshots of drop profiles are given at different stages of a stick-slip cycle (times given above panels) for a drop depinning from a hydrophilic line defect (marked by the horizontal line). The driving $\mu = 5.193 \cdot 10^{-3}$ is close to the critical μ_c. Colour code and remaining parameters are as in fig. 3.

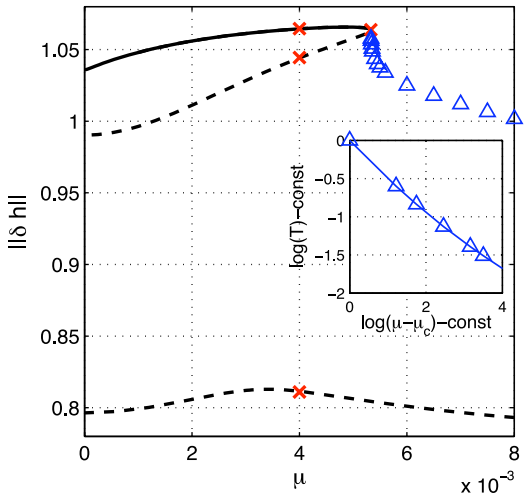

Fig. 5: (Colour on-line) Bifurcation diagram for drops pinned by a hydrophobic defect at $\epsilon = 0.3$ and $H = 1.2$. The presented norms, line styles, symbols, domain size and inset are as in fig. 2. Profiles at the crosses are given in fig. 6. The straight line in the inset corresponds to a power law with exponent $-1/2$.

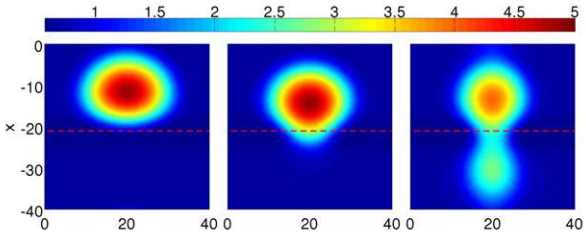

Fig. 6: (Colour on-line) Shown are contours of steady-drop solutions for a hydrophobic defect for $\mu = 4 \cdot 10^{-3}$. From left to right, profiles correspond to crosses in fig. 5 from large to small norm. That is, the left panel shows the stable pinned drop. The thin line marks the minimum of wettability.

It becomes higher and more oval with increasing μ as it is increasingly pushed against the defect. In consequence, its norm increases up to very close to the depinning transition at μ_c. A typical profile is given in the left panel of fig. 6. There exist two unstable solutions even for $\mu = 0$ (dashed lines in fig. 5). One of them "annihilates" with the stable one at the saddle-node bifurcation, whereas the other one continues towards large driving. Typical profiles are given in the middle and right panel of fig. 6, respectively. Both unstable drops are situated mainly upstream of the defect but have downstream protrusions that reach beyond the defect. Drops on the middle branch correspond to threshold solutions similar to the hydrophilic case. Time simulations indicate that depinning occurs again *via* a SNIPER bifurcation, *i.e.*, a branch of time-periodic solutions emerges at μ_c. However, the T on $(\mu - \mu_c)$ dependence (inset of fig. 5) slightly deviates from the $-1/2$ power law even at only 0.5% distance from μ_c. This difference to the hydrophilic case results from the closeness in parameter space of a higher co-dimension critical point.

A time series of snapshots for a stick-slip motion of a depinned drop is given in fig. 7. The depinning process is rather different from the hydrophilic 3d case and, indeed, from the 2d case: The drop first lets a "protrusion" slowly creep over the defect. This takes about 3600 time units (snapshots 1 and 2). Then within 650 units it depins and slides to the next defect (snapshots 2 to 5), where it needs another 5000 units to reach the state as in snapshot 1 (snapshots 5 and 6). Then the cycle starts again. Once the drop is depinned, a small drop is retained behind the defect (snapshot 4).

It is interesting to note that the individual stations of a stick-slip motion that can be seen in figs. 4 and 7 do very much resemble the unstable steady solutions presented in figs. 3 and 6, respectively. This indicates that the steady solutions that exist at $\mu < \mu_c$ are above μ_c still present in the phase space as "ghost solutions" [27] and can be seen in the course of the time-periodic motion.

Next, we elucidate the character of the single steady-state solution that remains for large μ for both hydrophilic and hydrophobic defects. Continuation far beyond the range of figs. 2 and 5, respectively, shows that in the 3d case the norm approaches a finite value, *i.e.*, there remains a non-trivial large amplitude structure. This is in stark contrast to the 2d case where the norm approaches zero and the solutions resemble slightly modulated films. We show in fig. 8 that in the 3d case equally for hydrophilic as for hydrophobic defects this solution branch consists of rivulet states with drop-like transverse cross sections and comparatively small variation in streamwise direction. The latter become even smaller with increasing driving. It is interesting to note that the rivulet becomes linearly stable at a large finite driving μ_r. It stabilises *via* a Hopf

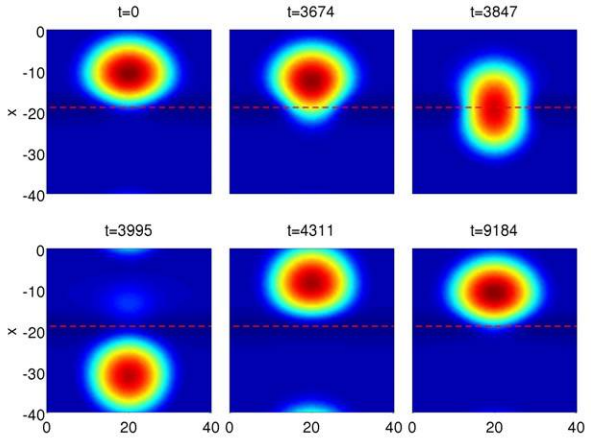

Fig. 7: (Colour on-line) Snapshots of drop profiles are given at different stages of a stick-slip cycle for a drop depinning from a hydrophobic line defect (marked by the horizontal line). The driving ($\mu = 5.331 \cdot 10^{-3}$) is close to the critical one. Colour code and remaining parameters are as in fig. 6.

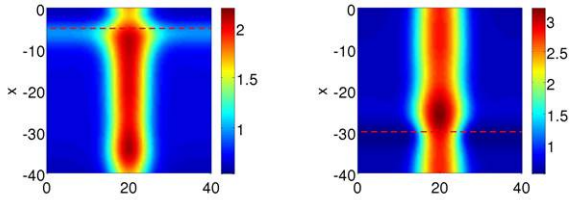

Fig. 8: (Colour on-line) Shown are contours of steady rivulet solutions for large driving force $\mu = 0.03$ for (left) hydrophilic and (right) hydrophobic defects. The remaining parameters are as in figs. 2 and 5, respectively. The horizontal lines mark the extrema of wettability.

bifurcation where it is joined by the branch of time-periodic solutions. This behaviour has no counterpart in 2d.

Finally, we investigate the influence of the load on depinning by varying the drop volume V for fixed domain size. We quantify V by the difference of mean height H and precursor film thickness H_p. In particular, here $V = 1600(H - H_p)$. As the depinning mechanism *via* SNIPER bifurcation remains the dominant one when increasing the drop volume, we characterise the load at depinning in fig. 9 by the dependence of the critical driving on volume.

With increasing load (*i.e.*, drop volume), depinning occurs at smaller critical driving μ_c. The accompanying bifurcation diagrams resemble fig. 5 but with an increasingly pointed fold. The dependencies in fig. 9 are well fitted by power laws $\mu_c \sim (H - H_p)^{-\alpha}$ with $\alpha \approx 3/4$. The exact value depends slightly on the type of defect: we find $\alpha \simeq 0.72$ (hydrophobic) and $\alpha \simeq 0.76$ (hydrophilic). At equal drop volume, an about 30% larger driving force is needed for depinning from the hydrophobic than from the hydrophilic defect. This applies to the 2d and the 3d case.

Furthermore, one notices a small systematic difference between the 2d and the 3d case: for identical droplet

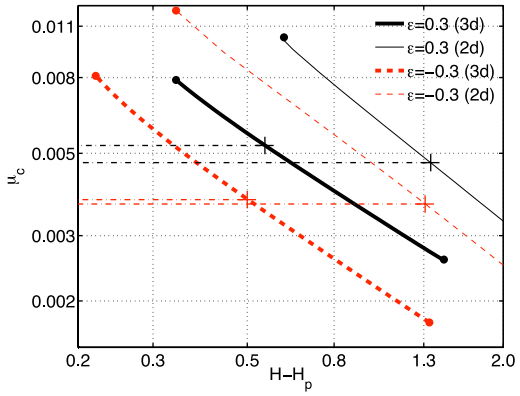

Fig. 9: (Colour on-line) Shown is the load at depinning by a SNIPER bifurcation as indicated by the dependence of the critical driving μ_c on drop volume as represented by $H - H_p$. The log-log plot gives the cases of hydrophilic (dashed lines) and hydrophobic (solid lines) in the 3d (heavy lines) and the 2d (thin lines) case. The defect strength is fixed as given in the legend. Symbols "+" indicate a set of drops that have identical height at $\mu = 0$. Beyond the ends of the lines, other depinning mechanisms dominate.

height, the critical driving in the 3d case is slightly larger than the 2d one. Our interpretation is that the difference results mainly from a lower "effective 2d loading" in the 3d case (*i.e.*, smaller mass per lateral length of the drop).

When the lines in fig. 9 end in black circles, this indicates that beyond the corresponding μ a different mechanism is dominant. The related complex changes in the bifurcation scenario will, however, be discussed in detail elsewhere. Here, we give a brief description only. For small drops, the flow in the precursor film becomes important and might trigger a depinning *via* a Hopf bifurcation in the 2d (see [14]) as well as in the 3d case. Beyond depinning a stick-slip motion is found; however, the period does tend to a finite value as one approaches μ_c from above. For the present parameter values, such a mechanism is found for the hydrophobic and hydrophilic case.

For large drops, the 2d case always shows a SNIPER scenario of depinning. In the 3d case, the process may become more involved as a possible coexistence of a ridge and a drop solution with identical volume comes into play. In consequence, the Rayleigh instability of a ridge may couple to the depinning instability studied here. As a result, one finds a richer behaviour, *e.g.*, the formation of fingers and transitions between ridges, drops and rivulets.

Conclusion. – We have studied depinning three-dimensional drops under lateral driving for localised hydrophobic and hydrophilic line defects employing on the one hand continuation techniques to obtain steady-state solutions (pinned drops and rivulets) and their stability and on the other hand a time-stepping algorithm to study the dynamics of the stick-slip motion beyond depinning. As a result, we have found that for the

parameter range we have mainly focused on, the depinning behaviour seems at first sight to be qualitatively very similar in the 2d and the 3d case: Drops are pinned up to a critical driving μ_c where they depin *via* a SNIPER bifurcation as indicated in bifurcation diagrams like figs. 2 and 5. In the limiting case of small drops, depinning occurs *via* a Hopf bifurcation. In this limit, drops are only four or five times higher than the precursor film and depinning is caused by the flow in the wetting layer. For realistic forces, the effect cannot be observed for partially wetting nano- or micro-drops on an incline or rotating disc and we have not considered the parameter regime here. Note, however, that micro-drops of dielectric liquids generated by an electric field in a capacitor can coexist with a thick wetting layer of 100 nm to 1 μm stabilised by van der Waals interaction [28,29]. In such a setting, both depinning mechanisms should be observable using gravity as the driving force. A calculation in the 2d case is given in the appendix of [13].

The SNIPER bifurcation we have focused on is characterised by a square-root power law dependence of the inverse time scale of depinning on the distance from threshold $\mu - \mu_c$. Beyond μ_c, the unsteady motion resembles the stick-slip motion observed in experiment: The advance of the drop is extremely slow when overcoming the influence of the defect, and very fast once it has broken away and slides to the next defect. This general agreement of 2d and 3d case corroborates the often voiced expectancy that studies of two-dimensional thin film systems can be employed to deduct many properties of physically more realistic three-dimensional systems. To show this has been an important aim of the present work.

However, beside the common general picture we have as well found significant qualitative differences mostly related to the additional degrees of freedom that the 3d system has. They allow the 3d drop to employ pathways of morphological changes for depinning that a 2d drop is not able to access. In particular, they allow the drop to "probe" barriers locally by sending an advancing protrusion over the defect (in the hydrophobic case) or by gradually thinning the backward thread that connects it to the defect (in the hydrophilic case). A short glance at the presented actual steady and non-steady drop profiles shows that they represent truly three-dimensional drops entirely different from 2d ones. Other significant differences are the existence of stable rivulets that do not exist in 2d and the mentioned coupling of Rayleigh and depinning instabilities that will be the subject of future studies.

* * *

We acknowledge support by the EU [MRTN-CT-2004005728 (PATTERNS); PITN-GA-2008-214919 (MULTIFLOW)] and the DFG [SFB 486, B13].

REFERENCES

[1] Podgorski T., Flesselles J.-M. and Limat L., *Phys. Rev. Lett.*, **87** (2001) 036102.
[2] Thiele U., Velarde M. G., Neuffer K., Bestehorn M. and Pomeau Y., *Phys. Rev. E*, **64** (2001) 061601.
[3] Snoeijer J. H., Le Grand N., Limat L., Stone H. A. and Eggers J., *Phys. Fluids*, **19** (2007) 042104.
[4] Thiele U., Neuffer K., Bestehorn M., Pomeau Y. and Velarde M. G., *Colloids Surf. A*, **206** (2002) 87.
[5] Schäffer E. and Wong P. Z., *Phys. Rev. Lett.*, **80** (1998) 3069.
[6] Tavana H., Yang G. C., Yip C. M., Appelhans D., Zschoche S., Grundke K., Hair M. L. and Neumann A. W., *Langmuir*, **22** (2006) 628.
[7] Golestanian R. and Raphaël E., *Europhys. Lett.*, **55** (2001) 228.
[8] Robbins M. O. and Joanny J. F., *Europhys. Lett.*, **3** (1987) 729.
[9] de Gennes P.-G., *Rev. Mod. Phys.*, **57** (1985) 827.
[10] Leger L. and Joanny J. F., *Rep. Prog. Phys.*, **55** (1992) 431.
[11] Quéré D, Azzopardi M. J. and Delattre L., *Langmuir*, **14** (1998) 2213.
[12] Spelt P. D. M., *J. Fluid Mech.*, **561** (2006) 439.
[13] Thiele U. and Knobloch E., *New J. Phys.*, **8** (2006) 313, 1.
[14] Thiele U. and Knobloch E., *Phys. Rev. Lett.*, **97** (2006) 204501.
[15] Oron A., Davis S. H. and Bankoff S. G., *Rev. Mod. Phys.*, **69** (1997) 931.
[16] Kalliadasis S. and Thiele U. (Editors), *Thin Films of Soft Matter, CISM Int. Centre Mech. Sci. Ser.*, Vol. **490** (Springer, Wien, New York) 2007.
[17] Sharma A., *Langmuir*, **9** (1993) 861.
[18] Thiele U., *Eur. Phys. J. E*, **12** (2003) 409.
[19] Beltrame P. and Thiele U., preprint, `http://arxiv.org/abs/0903.0014` (2008).
[20] Teletzke G. F., Davis H. T. and Scriven L. E., *Rev. Phys. Appl.*, **23** (1988) 989.
[21] Thiele U., Velarde M. G. and Neuffer K., *Phys. Rev. Lett.*, **87** (2001) 016104.
[22] Doedel E., Paffenroth R., Champneys A., Fairgrieve T., Kuznetsov Y., Sandstede B. and Wang X., Technical Report Caltech (2001).
[23] Bertozzi A. L., Grün G. and Witelski T. P., *Nonlinearity*, **14** (2001) 1569.
[24] Becker J. and Grün G., *J. Phys.: Condens. Matter*, **17** (2005) S291.
[25] Friesner R. A., Tuckerman L. S., Dornblaser B. C. and Russo T. V., *J. Sci. Comput.*, **4** (1989) 327.
[26] Thiele U., Brusch L., Bestehorn M. and Bär M., *Eur. Phys. J. E*, **11** (2003) 255.
[27] Strogatz S. H., *Nonlinear Dynamics and Chaos* (Addison-Wesley) 1994.
[28] Lin Z., Kerle T., Baker S. M., Hoagland D. A., Schäffer E., Steiner U. and Russell T. P., *J. Chem. Phys.*, **114** (2001) 2377.
[29] Merkt D., Pototsky A., Bestehorn M. and Thiele U., *Phys. Fluids*, **17** (2005) 064104.